Magnetic Resonance in Medicine 52:965–978 (2004)

New Modeling and Experimental Framework to Characterize Hindered and Restricted Water Diffusion in Brain White Matter

Yaniv Assaf,[1,2] Raisa Z. Freidlin,[3] Gustavo K. Rohde,[4] and Peter J. Basser[3]

To characterize anisotropic water diffusion in brain white matter, a theoretical framework is proposed that combines hindered and restricted models of water diffusion (CHARMED) and an experimental methodology that embodies features of diffusion tensor and *q*-space MRI. This model contains a hindered extra-axonal compartment, whose diffusion properties are characterized by an effective diffusion tensor, and an intra-axonal compartment, whose diffusion properties are characterized by a restricted model of diffusion within cylinders. The hindered model primarily explains the Gaussian signal attenuation observed at low *b* values; the restricted non-Gaussian model does so at high *b*. Both high and low *b* data obtained along different directions are required to estimate various microstructural parameters of the composite model, such as the nerve fiber orientation(s), the T_2-weighted extra- and intra-axonal volume fractions, and principal diffusivities. The proposed model provides a description of restricted diffusion in 3D given by a 3D probability distribution (average propagator), which is obtained by 3D Fourier transformation of the estimated signal attenuation profile. The new model is tested using synthetic phantoms and validated on excised spinal cord tissue. This framework shows promise in determining the orientations of two or more fiber compartments more precisely and accurately than with diffusion tensor imaging. Magn Reson Med 52: 965–978, 2004. Published 2004 Wiley-Liss, Inc.†

Key words: MRI; white matter; DTI; *q*-space

The advent of diffusion magnetic resonance imaging (MRI) methods has advanced the field of neuroimaging, particularly the radiologic assessment of white matter patency, microstructure, architectural organization, and orientation (1–4).

Neuronal tissue in general and white matter in particular are heterogeneous on a microscopic scale. Axons are ordered in fascicles surrounded by a complex extra-axonal environment containing astrocytes, glia, and ordered and randomly oriented extracellular matrix molecules. This heterogeneity makes it difficult to characterize white matter radiologically since each compartment can, in principle, contribute to the measured MRI signal. Despite this heterogeneity, diffusion properties in coherent white matter pathways exhibit diffusion anisotropy with highest apparent diffusivity measured along the fiber axes and the lowest perpendicular to them. It is still not clear whether the observed diffusion anisotropy arises from the intra-axonal compartment (primarily restricted diffusion) or the extra-axonal compartment (primarily hindered diffusion) or some combination thereof.

Several modeling and/or experimental approaches have been proposed to describe and/or characterize anisotropic diffusion observed in brain white matter. The first integrated experimental and modeling framework proposed to describe diffusion anisotropy was DTI (4), which is based on a Gaussian model of the random displacements of water molecules in an excited volume. The effective diffusion tensor estimated using this method represents a powder average over all individual microdomains and microenvironments within a voxel (5). So, while the macroscopic diffusion tensor, **D**, reflects the architectural features in tissues with a coherently organized microstructure (e.g., diffusion anisotropy, fiber orientation), **D** only represents a consensus average from individual compartments in regions with a heterogeneous fiber architecture, for example, where fibers cross (see (6) for a more detailed explanation) (5–7).

A number of detailed numerical models have been advanced to explain the macroscopic diffusion attenuation behavior observed in gray and white matter (8). These models use Monte Carlo simulations in tissue domains with assumed microstructure and architecture.

More recently, advances in imaging gradient hardware have allowed high *b*-value diffusion weighted imaging (DWI) data to be acquired, revealing "non-mono-exponential" behavior of the signal attenuation (9–11), especially in white matter. This finding has prompted some to extend the original DTI model to contain two or more diffusion tensors, which can be estimated from DWI data (9,12–14). In these works, it is assumed that the "fast" (or rapidly decaying) diffusion component can be associated with the extracellular space, and the "slow" (or slowly decaying) diffusion component can be associated with the intracellular space. However, if this slowly diffusing component arises from restricted diffusion (a non-Gaussian process), fitting the overall signal decay to a bi- or multiexponential tensor model, which assumes Gaussian diffusion, is inappropriate (15,16).

Other attempts to describe DWI data obtained from white matter employ *q*-space methods, originally pro-

[1]Functional Brain Imaging Unit, The Wohl Institute for Advanced Imaging, Tel Aviv Sourasky Medical Center, Tel Aviv, Israel.

[2]School of Chemistry, Tel Aviv University, Ramat Aviv, Tel Aviv, Israel.

[3]Telemedicine and Applied Imaging Section, Computational Bioscience and Engineering Laboratory, Center for Information Technology, The National Institutes of Health, Bethesda, Maryland.

[4]Section on Tissue Biophysics and Biomimetics, Laboratory of Integrative and Medical Biophysics, National Institute of Child Health and Human Development, The National Institutes of Health, Bethesda, Maryland.

*Correspondence to: Yaniv Assaf, Functional Brain Imaging Unit, The Wohl Institute for Advanced Imaging, Department of Radiology, Tel Aviv Sourasky Medical Center, Tel Aviv 64239, Israel. E-mail: asafyan@zahav.net.il

Received 24 November 2003; revised 2 April 2004; accepted 3 April 2004.

2004 ISMRM Young Investigator I.I. Rabi finalist.

DOI 10.1002/mrm.20274

Published online in Wiley InterScience (www.interscience.wiley.com).

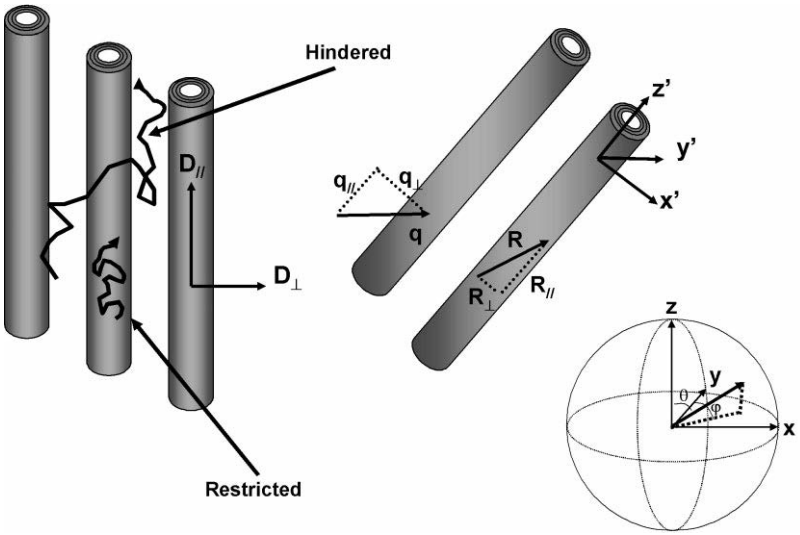

FIG. 1. The modeling framework showing the two modes of diffusion in white matter, hindered outside the cylinders and restricted within the cylinders. Diffusion in the hindered part is characterized by a diffusion tensor. Diffusion in the restricted part can be decomposed into diffusivities parallel and perpendicular to the cylinder's axis ($D_{//}$ and $D_{\perp}$). In the same manner, the reciprocal wavenumber vector, $\mathbf{q}$, can be decomposed into $\mathbf{q}_{//}$ and $\mathbf{q}_{\perp}$ with respect to the fiber axis. The spherical coordinate system as shown on the right is used to relate measured quantities in the laboratory frame to computed quantities in the "fiber" frame of reference.

posed by Callaghan (17) and Cory and Garroway (18). In this approach, no specific model of water diffusion is assumed. Instead, features of the measured displacement probability distribution are extracted by a Fourier transformation of the signal attenuation profile with respect to q (the reciprocal wavenumber defined as $\gamma\delta g/2\pi$ where γ is the gyromagnetic ratio, δ is the diffusion gradient duration, and g is the diffusion gradient amplitude). Biologic and clinical examples include applications in ischemia (19), in studying normal white matter structure (12,20–22) and diseased neuronal and human brain tissues (20–22).

A primary contribution of the q-space methodology is the demonstration that the slow diffusing components observed at high q (or b) values result from restricted diffusion, probably in the intra-axonal compartment (16). While existing q-space MR methods may provide, under certain experimental conditions, a displacement profile along a specific measured direction (23) or a 3D displacement distribution function (12,17), they do not provide microstructural parameters such as the intra-axonal and extra-axonal fractions or their principal diffusivities and directions. A mathematical model of the water diffusion process in tissues is needed in order to extract this information.

Here we propose a hybrid modeling framework that embodies analytical models of both hindered and restricted diffusion in white matter (composite hindered and restricted model of diffusion, CHARMED) and an experimental methodology that combines aspects of diffusion tensor MRI and q-space MRI. We propose a model of white matter that contains a hindered extra-axonal region, whose diffusion properties are characterized by an effective diffusion tensor, and a restricted model of diffusion in the intra-axonal space. We combine these descriptions and show how to use DWI data to estimate various microstructural parameters of this model, such as fiber orientation, the T_2-weighted fractions of extra and intra-axonal spaces, and intra-axonal diffusivity, as well as the net displacement distribution produced by water diffusing in both compartments.

THEORY

General Description

The model of water diffusion in white matter ascribes the MR signal attenuation to two processes: hindered water diffusion in the extra-axonal space and restricted water diffusion in the intra-axonal space (Fig. 1). Because exchange between the two compartments should be extremely slow in relation to the experimental time scale, we use the "slow exchange" limit[5] (24). Then, the net measured signal attenuation, $E(\mathbf{q},\Delta)$, is given by the weighted sum of the two contributions:

$$E(\mathbf{q}, \Delta) = f_h \cdot E_h(\mathbf{q}, \Delta) + f_r \cdot E_r(\mathbf{q}, \Delta). \quad [1]$$

Above, f_{h} and f_{r} are the T_2-weighted volume fractions of the hindered and restricted compartments, respectively, Δ is the diffusion time, and $E_{\mathrm{h}}(\mathbf{q},\Delta)$ and $E_{\mathrm{r}}(\mathbf{q},\Delta)$ are the normalized MR echo signals from the hindered and restricted compartments, respectively.

Decoupling Diffusive Motions in the Restricted Compartment

One important simplification of the proposed model is that $E_{\mathrm{r}}(\mathbf{q},\Delta)$ above can further be decomposed into contributions arising from spins diffusing parallel and perpendicular to the axon's axis. To see this, we first apply the relationship between $E_{\mathrm{r}}(\mathbf{q},\Delta)$ and the average propagator, $\bar{P}_s(\mathbf{R}, \Delta)$, at diffusion time, Δ (17,25):

$$E_r(\mathbf{q}, \Delta) = \iiint \bar{P}_s(\mathbf{R}, \Delta) e^{2\pi i \mathbf{q}\cdot\mathbf{R}}\, d\mathbf{R} \quad \text{where } \mathbf{q} = \frac{\gamma \mathbf{g} \delta}{2\pi}. \quad [2]$$

Above, $\mathbf{R}$ is the net displacement vector for a spin, γ is the proton gyromagnetic ratio, $\mathbf{g}$ is the vector whose magni-

[5]The corresponding fast exchange limit can be written as a volume fraction weighted expression, $E(\mathbf{q}, \Delta) = E_h(q, \Delta)^{f_h} \times E_r(q, \Delta)^{f_r}$.

tude is the strength of the applied diffusion gradient and whose direction is along the axis of the applied diffusion gradient, δ is the width of the diffusion pulse gradient, and Δ is the diffusion time.

Second, we note that solutions to the diffusion equation in restricted cylinders and sheets (17,26–30) factor into products of *x*-, *y*-, and *z*-dependent terms when viewed in the principal coordinate frame of reference. In these systems, displacements perpendicular to restricted boundaries do not affect displacements parallel to them. This point is developed in detail in Appendix D.

$$\bar{P}_s(\mathbf{R}, \Delta) = \bar{P}_\perp(\mathbf{R}_\perp, \Delta)\bar{P}_{//}(\mathbf{R}_{//}, \Delta), \quad [3]$$

where $\mathbf{R}$ is the net displacement vector, and $\bar{P}_{//}(\mathbf{R}, \Delta)$ and $\bar{P}_\perp(\mathbf{R}, \Delta)$ are the displacement probability propagators for motion in the parallel and perpendicular directions, respectively.

Next, we note that any $\mathbf{R}$ can be decomposed into displacement vectors parallel to the axon's axis and perpendicular to it, i.e., $\mathbf{R} = \mathbf{R}_{//} + \mathbf{R}_\perp$. Also, any $\mathbf{q}$ that we apply in the laboratory frame can likewise be written as a sum of vectors parallel and perpendicular to the axon's axis: i.e., $\mathbf{q} = \mathbf{q}_{//} + \mathbf{q}_\perp$. We define the MR signals arising from motion solely in the perpendicular and parallel directions, respectively, $E_\perp(\mathbf{q}_\perp)$ and $E_{//}(\mathbf{q}_{//})$, as[6]

$$E_\perp(\mathbf{q}_\perp) = \iint \bar{P}_\perp(\mathbf{R}_\perp, \Delta)e^{2\pi i\mathbf{q}_\perp\cdot\mathbf{R}_\perp}\, d\mathbf{R}_\perp \quad \text{and}$$

$$E_{//}(\mathbf{q}_{//}) = \int \bar{P}_{//}(\mathbf{R}_{//}, \Delta)e^{2\pi i\mathbf{q}_{//}\cdot\mathbf{R}_{//}}\, d\mathbf{R}_{//} \quad [4]$$

and then we see in Appendix A that Eq. [2] can be written compactly as

$$E_r(\mathbf{q}, \Delta) = E_\perp(\mathbf{q}_\perp, \Delta)E_{//}(\mathbf{q}_{//}, \Delta). \quad [5]$$

Thus, statistical independence of displacements along the axial and radial directions within the axon implies that $E_r(\mathbf{q},\Delta)$ can be expressed as the *product* of MR signals arising from displacements parallel and perpendicular to the axon's main axis.

The Form of $E_{//}(\mathbf{q}_{//},\Delta)$ in the Restricted Compartment

For displacements parallel to the axis of the fiber we assume free 1D Gaussian diffusion, having diffusivity, $D_{//}$,

$$P_{//}(\mathbf{R}_{//}, \Delta) = \frac{1}{\sqrt{4\pi D_{//}\left(\Delta - \frac{\delta}{3}\right)}}\, e^{-|\mathbf{R}_{//}|^2/(4D_{//}(\Delta-(\delta/3)))}. \quad [6]$$

Fourier transformation of Eq. [6] (as in Eq. [2]) leads to Stejskal's familiar equation,

$$E_{//}(\mathbf{q}_{//}, \Delta) = e^{-4\pi^2|\mathbf{q}_{//}|^2(\Delta-(\delta/3))D_{//}}. \quad [7]$$

Equation [7] specifies the form of $E_{//}(\mathbf{q}_{//},\Delta)$ in Eq. [5] above.

The Form of $E_\perp(\mathbf{q}_\perp,\Delta)$ in the Restricted Compartment

Expressions for $E_\perp(\mathbf{q}_\perp,\Delta)$ for diffusion in a restricted cylinder of radius R can be found in Codd and Callaghan's recent works (30). These, however, apply when the narrow pulse or pulse-field gradient approximation holds (i.e., $\delta \sim 0$ and $\delta \ll \Delta$). An approximation that is more mathematically tractable and that more faithfully represents experimental conditions in clinical and biologic DWI applications in which $\delta \sim \Delta$ is that the diffusion gradient waveform is a constant. Thus, we use an asymptotic form of $E_\perp(\mathbf{q}_\perp,\Delta)$ for restricted diffusion in a cylinder proposed by Neuman (29) under the assumption of a constant field gradient,

$$E_\perp(\mathbf{G}_\perp, 2\tau) = e^{-(R^4\gamma^2G_\perp^2/D_\perp)(7/96)(2\tau-(99/112)(R^2/D_\perp))}. \quad [8]$$

Above, $D_\perp$ is the intra-axonal diffusivity perpendicular to the fiber axis (which can be different from $D_{//}$ in Eq. [6]), and 2τ is the echo time (TE) of the acquisition. This expression can be rewritten in terms of $\mathbf{q}_\perp$,

$$E_\perp(\mathbf{q}_\perp, 2\tau) = e^{-(4\pi^2R^4|\mathbf{q}_\perp|^2/D_\perp\tau)(7/96)(2-(99/112)(R^2/D_\perp\tau))}. \quad [9]$$

In contrast to Callaghan's formula, which may give the diffraction pattern in the signal decay formed by the restricted barriers of the cylinders, Neuman's formula yields only a multiexponential signal decay. This is expected since gradient pulses that are "fat" or wide blur the diffraction pattern. An alternative model to Eq. [9] that can account for the finite width of the diffusion gradient pulse is given by van Gelderen et al. (31). Finally, to obtain an expression for $E_r(\mathbf{q},\Delta)$ in Eq. [5], we substitute Eqs. [7] and [9],

$$E_r(\mathbf{q}, \Delta) = e^{-4\pi^2|\mathbf{q}_{//}|^2(\Delta-(\delta/3))D_{//}} \cdot e^{-(4\pi^2R^4|\mathbf{q}_\perp|^2/D_\perp\tau)(7/96)(2-(99/112)(R^2/D_\perp\tau))}. \quad [10]$$

Equation [10] specifies the form of the restricted compartment for an array of bundles of radius R.

The Form of $E_h(\mathbf{q},\Delta)$ in the Hindered Compartment

We assume that diffusion in the extra-axonal compartment, which consists of astrocytes, glia, and extracellular matrix, is hindered and, thus, that this compartment has a 3D Gaussian displacement distribution. In general, this diffusion process is assumed to be anisotropic and characterized by an effective diffusion tensor, $\mathbf{D}$ (32),

$$E_h(\mathbf{q}, \Delta) = e^{-4\pi^2(\Delta-(\delta/3))\mathbf{q}^TD\mathbf{q}}, \quad [11]$$

where $\mathbf{q}^T$ is the matrix transpose of $\mathbf{q}$. We further assume that anisotropic diffusion in the hindered compartment is caused by reflections from and increased tortuosity pro-

[6]The double integral indicates that we perform the integration over the tube cross section, while the single integral is performed along the axon's axis.

duced by axons (and possibly neurofilaments and proteins in the extracellular space oriented parallel to them). Therefore, we would expect that the principal axes of **D** are coincident with the parallel and perpendicular axes of the restricted compartment in the case of a single bundle of uniformly oriented fibers.[7] We test this hypothesis experimentally below.

Again, taking into account that $\mathbf{q} = \mathbf{q}_{//} + \mathbf{q}_{\perp}$, we simplify the quadratic form in Eq. [11], as in Appendix C. Inserting Eq. [C2] into Eq. [11] gives[8]

$$E_h(\mathbf{q}, \Delta) = e^{-4\pi^2(\Delta-(\delta/3))(|\mathbf{q}_{\perp}|^2\lambda_{\perp}+|\mathbf{q}_{//}|^2\lambda_{//})}, \quad [12]$$

which can be rewritten as

$$E_h(\mathbf{q}, \Delta) = e^{-4\pi^2(\Delta-(\delta/3))|\mathbf{q}_{\perp}|^2\lambda_{\perp}} \cdot e^{-4\pi^2(\Delta-(\delta/3))|\mathbf{q}_{//}|^2\lambda_{//}}. \quad [13]$$

Interestingly, just as for Eq [5] above describing diffusion in the intra-axonal compartment, one can infer that in the principal frame of the hindered compartment diffusive motion parallel and perpendicular to the principal directions of the axon are also statistically independent.

Composite Model for One Restricted and One Hindered Compartment

Referring to Eqs. [1], [10], and [12] the composite model of the net MR signal is a weighted sum of contributions from the restricted and hindered compartments,

$$E(\mathbf{q}, \Delta) = f_h \cdot e^{-4\pi^2(\Delta-(\delta/3))(|\mathbf{q}_{\perp}|^2\lambda_{\perp}+|\mathbf{q}_{//}|^2\lambda_{//})} + f_r \cdot e^{-4\pi^2|\mathbf{q}_{//}|^2(\Delta-(\delta/3))D_{//}-(4\pi^2R^4|\mathbf{q}_{\perp}|^2/D_{\perp}\tau)(7/96)(2-(99/112)(R^2/D_{\perp}\tau))}. \quad [14]$$

Composite Model for Multiple Restricted and Hindered Compartments

It is straightforward to extend Eq. [1] to consider multiple restricted and hindered compartments,

$$E(\mathbf{q}, \Delta) = \sum_{i=1}^{M} f_h^i \cdot E_h^i(q, \Delta) + \sum_{j=1}^{N} f_r^j \cdot E_r^j(q, \Delta). \quad [15]$$

Here, M is the number of distinct hindered compartments and N is the number of distinct restricted compartments, which are not necessarily the same. In Eq. [15] it is still assumed that during the period of the MR experiment, there is no exchange between compartments.

It has been shown previously that $E(\mathbf{q})$ has a characteristic quadratic decay behavior in the low-q regime (33),

$$E(\mathbf{q}, \Delta) \approx 1 - 4\pi^2\mathbf{q}^T\mathbf{D}\mathbf{q}\left(\Delta - \frac{\delta}{3}\right). \quad [16]$$

Moreover, it has been shown that at low-q values, **D** represents a powder average of all diffusion tensors in the various hindered subcompartments (7), and thus, it should be sufficient to characterize the hindered compartment in Eq. [15] by a single hindered compartment with a single effective diffusion tensor (i.e., $M = 1$ above),

$$E(\mathbf{q}, \Delta) = f_h \cdot E_h(q, \Delta) + \sum_{j=1}^{N} f_r^j \cdot E_r^j(q, \Delta). \quad [17]$$

Here it is useful to assume the most general form of the diffusion tensor describing the hindered compartment given in Eq. [11].

Johnson Noise

In these experiments, where the attenuation caused by diffusion can be substantial, the signal caused by background or Johnson noise must be modeled,

$$E(\mathbf{q}, \Delta) = \sqrt{\left(\sum_{i=1}^{M} f_h^i \cdot E_h^i(q, \Delta) + \sum_{j=1}^{N} f_r^j \cdot E_r^j(q, \Delta)\right)^2 + \eta^2}. \quad [18]$$

Here we account for the fact that the MR signal we measure is in the presence of rectified Gaussian noise. The variable η is the background noise level that is estimated as an additional free parameter as in Refs. (34,35).

Relating the Laboratory and Principal Frames of Reference

Finally, we need to relate the vector **q** applied in the laboratory frame of reference to $\mathbf{q}_{//}$ and $\mathbf{q}_{\perp}$, vectors in the directions parallel and perpendicular to the axis of the axon, respectively. These formulae are given in Appendix B.

METHODS

Simulated Data

Simulated signal decay data were generated using the models described above. The signal decay was produced using Eq. [15], which combines multiple hindered and restricted compartments. Noise was added in quadrature and then rectified, as explained in Ref. (35). Simulated signal decay for a single fiber model was obtained by simulating one hindered and one restricted component ($M = N = 1$ in Eq. [15]). The signal decay for the two-fiber model was produced by combining two sets of hindered and restricted compartments ($M = N = 2$ in Eq. [15]). Input parameters for the signal decay simulation were population fraction of each of the compartments, orientation of the restricted fiber(s) in a standard spherical coordinates system, the parallel and perpendicular diffusion coefficients of the hindered compartment(s) ($\lambda_{//}$ and $\lambda_{\perp}$), and the parallel and perpendicular diffusion coefficients of the restricted component ($D_{//}$ and $D_{\perp}$). The signal decay was simulated using several gradient direction schemes (Fig. 2a).

[7] In other words, the largest eigenvector of **D** is coincident with the axis of the restricted cylinders and the other two eigenvectors lie in a plane perpendicular to that direction.

[8] A facsimile of Eq. [13] was used by Boss and Stejskal (15) to model *restricted* diffusion between parallel plates, knowing beforehand that this form would be inadequate to describe restricted diffusion.

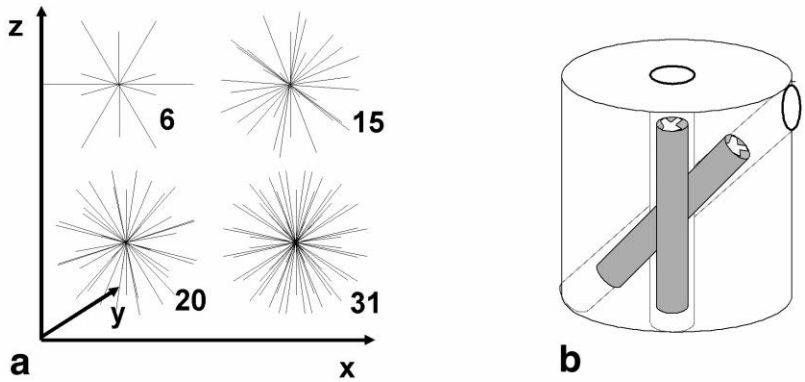

FIG. 2. (**a**) The diffusion gradient direction schemes used in simulations. Note that the 31-direction scheme was also used experimentally on the excised spinal cord. (**b**) A diagram of the experimental phantom used to generate images of crossing fibers. Two segments of freshly excised pig spinal cord were placed in a plastic tube so that one lies along the *z*-axis of the magnet and the other 45° off the *x*-axis. In regions where the two segments of the spinal cord crossed, we could simulate crossing fibers by making the slice thickness large enough to encompass both fiber populations.

Experimental Data

Excised spinal cords were scanned on a 7-T spectrometer (Bruker BioSpin. Inc.), equipped with a Micro2.5 gradient system with maximal gradient strength of 100 G/cm in three orthogonal directions. A spinal cord was freshly excised from a previously sacrificed pig. A section of the cervical spinal cord (2 cm) was cut in half; the two pieces were placed in the apparatus shown in Fig. 2b.

Diffusion experiments were performed using the pulsed gradient spin echo sequence with the following parameters: TR = 2000 msec, TE = 200 msec, Δ= 150 msec, δ = 40 msec. The field of view was 5 cm, matrix size was 64 × 64, and slice thickness was 15 mm, which was sufficient to include both sections of the crossed spinal cord specimen (see Fig. 2b). Pulsed gradients were incremented from 0 to 5.25 G/cm in 16 equal steps and measured in 31 noncollinear gradient directions (see Fig. 2a). The maximal *b* value in these experiments was approximately 44000 sec/mm^2 and the maximal *q* value was 89.4 mm^{-1}. Total number of images was 496; the acquisition time per direction was ~35 min and the total experimental time was about 18 hr.

Fitting Procedure

CHARMED presented in Eq. [15] was used to estimate microstructural parameters from diffusion data (simulated and experimental) using a nonlinear regression routine (employing the Levenberg–Marquardt minimization algorithm) in Matlab (The Mathworks). Four combinations of compartmental configurations were used.

1. One hindered and zero restricted compartments (M = 1; N = 0 in Eq. [15]) were used to fit a single fiber at low *b* values (standard diffusion tensor analysis of $b < 2500$ sec/mm^2). The number of free parameters for this combination was 7.

2. One hindered and zero restricted compartments (M = N = 1 in Eq. [15]) were used to fit a single fiber including high *b* values. The number of free parameters for this combination was 12.

3. Two hindered and zero restricted compartments (M = 2; N = 0 in Eq. [15]) were used to fit two crossing fibers at low *b* values (23). The number of free parameters in this case was 13.

4. One hindered and two restricted compartments (M = 1; N = 2 in Eq. [15]) were used to fit two crossing fibers including the high *b* value data. The number of free parameters in this case was 15.

Initial conditions for the low *b* value diffusion tensor based fitting (see combinations 1 and 3 above) were arbitrary and the same for all input data. Initial conditions for the high *b* value data (see combinations 2 and 4) were obtained from the diffusion tensor fitting (combination 1 above), which was performed prior to any of the other combinations. Thus, the direction(s) of the fiber(s) as derived from the low *b* value DTI analysis were taken as initial conditions for the restricted diffusion part.

Estimated parameters included the population fractions of the hindered and restricted multiple compartments, the eigenvectors and eigenvalues of the hindered part (as in conventional DTI), as well as $D_{//}$ of the restricted component, and the orientation of the restricted part in spherical coordinates. The noise floor, η, was also estimated in each fit. Two parameters were kept fixed through the fitting procedure: the fiber diameter distribution and the diffusion coefficient perpendicular to the long axis of the fibers ($D_\perp$). The fiber diameter distribution (incorporated into Eq. [9]) is typical for axons in spinal cord. The diffusion coefficient of the molecules perpendicular to the fibers was taken as 1×10^{-5} cm^2/sec. Once all parameters were estimated, we resampled $E(\mathbf{q})$ (by inverting Eq. [15]) on a uniform grid in *q*-space and obtained the 3D FFT, which corresponds to the 3D average propagator, $\bar{P}_s(\mathbf{R}, \Delta)$ (30). The 3D FFT matrices were then used to produce iso-probability surface plots or contours.

RESULTS

Simulated Data

The iso-probability plots reveal 3D shapes that are distinct from the familiar diffusion ellipsoid characteristic of 3D free anisotropic diffusion. Figure 3 shows the 3D FFT iso-probability plot of a single fiber having single restricted and hindered diffusion compartment aligned 30° below the *x* direction. The 3D FFT (i.e., the displacement distribution function) for the complete signal decay deviates significantly from the ellipsoidal shape. This deviation is reflected in the iso-probability plot of the total signal decay showing at least two distinct shapes (Fig. 3a). The decomposition of the signal decay using CHARMED provides the Gaussian part (hindered part, Fig. 3b) having the shape of

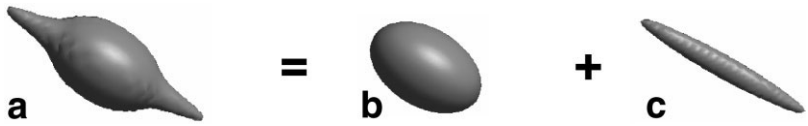

FIG. 3. (**a**) Displacement iso-probability plot obtained by taking the 3D FFT of the simulated signal decay for a single fiber aligned 30° below the *x*-axis. Simulations were performed using the following parameters for the hindered compartment: $f_h = 0.7$, $\Phi_h = -30°$, $\varphi_h = 90°$, $\lambda_1 = 0.8 \times 10^{-5}$ cm^2/sec, $\lambda_2 = \lambda_3 = 0.35 \times 10^{-5}$ cm^2/sec, and $f_r = 0.3$, $\Phi_r = -30°$, $\varphi_r = 90°$, $D_{//} = 1 \times 10^{-5}$ cm^2/sec for the restricted compartment. The noise floor in the simulations was 0.03. (**b**) Displacement iso-probability plot for the hindered compartment alone. (**c**) Displacement iso-probability plot for the restricted part alone.

an ellipsoid, and the non-Gaussian part (restricted part, Fig. 3c) having the shape of a toothpick. The 3D FFT iso-probability plot of the restricted part is much sharper and narrower than the hindered part. As CHARMED seem to provide higher angular definition of the fiber alignment, we conducted a series of Monte Carlo simulations aimed at estimating the bias and precision of the fiber alignment in 3D. For that purpose we resampled data (500 times) using the model (combination 1) for one fiber aligned along the *x*-axis. The data were resampled twice: once with *b* value of up to 14000 sec/mm^2 with 16 data points per direction (30 directions) and once with *b* value of up to 1000 sec/mm^2 with 16 data points per directions (again in 30 directions). For each sampling cycle we calculated the alignment of the fiber both using DTI model and both using CHARMED with one hindered and one restricted compartment. Using the 500 measurements we calculated the angle in which 95% of the measurement lies within (36). We found that for the DTI model the angle is 30.1° and that for the combined hindered-restricted model it is 10.1°.

The ability of the model to decompose the two components of the signal decay was tested for a single fiber as a function of the gradient sampling direction scheme. For that purpose we generated signal decay data for a fiber having a single hindered and single restricted compartment aligned 30° below the *x*-axis for diffusion gradient sampling schemes having 6, 15, 20, and 31 directions. The 3D FFT iso-probability shape associated with the restricted component is, as expected, narrower and more pointed than the hindered diffusion ellipsoid for all measured directions (Fig. 4). Visually, no major differences are seen among the different gradient schemes; indeed, fitting the signal decay at any measured direction produced similar results to the values used to produce the signal decay. However, the residuals to the fit for the 6-gradient direction scheme are almost threefold larger than those for the 31-direction scheme.

Separation of the hindered and restricted parts of the signal decay should be straightforward in the case of a single fiber due to the similar cylindrical geometry of both compartments. Yet, when two (or more) fiber bundles have different orientations, identifying them should be more difficult. Thus, we first tested the model's ability to separate two crossing fibers oriented at 90° with respect to each other. The corresponding diffusion signal decay was generated by simulating two fibers, each having its own hindered and restricted compartments ($M = N = 2$ in Eq. [15]). The simulated data were then fitted using two combinations of Eq. [15]: (a) two hindered compartments (i.e., a double tensor model) and (b) two restricted compartments and one hindered compartment. Figure 5 shows the 3D FFT iso-probability plots of the different models as a function of the number of sampling directions. The double tensor model was unable to produce the original 3D align-

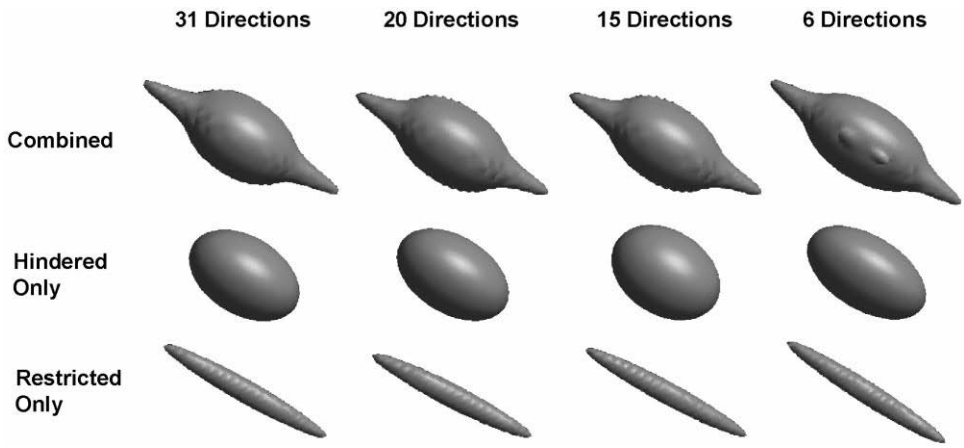

FIG. 4. The displacement iso-probability plots of a single fiber aligned at 30° below the *x*-axis as a function of the number of gradient directions (6, 15, 20, and 31 directions). The simulated signal decay was produced using Eq. [15] with one hindered and one restricted compartment. Parameters in the hindered compartment were $f_h = 0.7$, $\Phi_h = -30°$, $\varphi_h = 90°$, $\lambda_{//} = \lambda_1 = 0.8 \times 10^{-5}$ cm^2/sec, $\lambda_\perp = \lambda_2 = \lambda_3 = 0.35 \times 10^{-5}$ cm^2/sec. Parameters in the restricted compartment were: $f_r = 0.3$, $\Phi_r = -30°$, $\varphi_r = 90°$, $D_{//} = 1 \times 10^{-5}$ cm^2/sec. The noise floor in the simulations was 0.03. The contributions from the hindered and restricted compartments are shown separately as is their combined contribution, which is obtained from the 3D FFT of the entire signal decay.

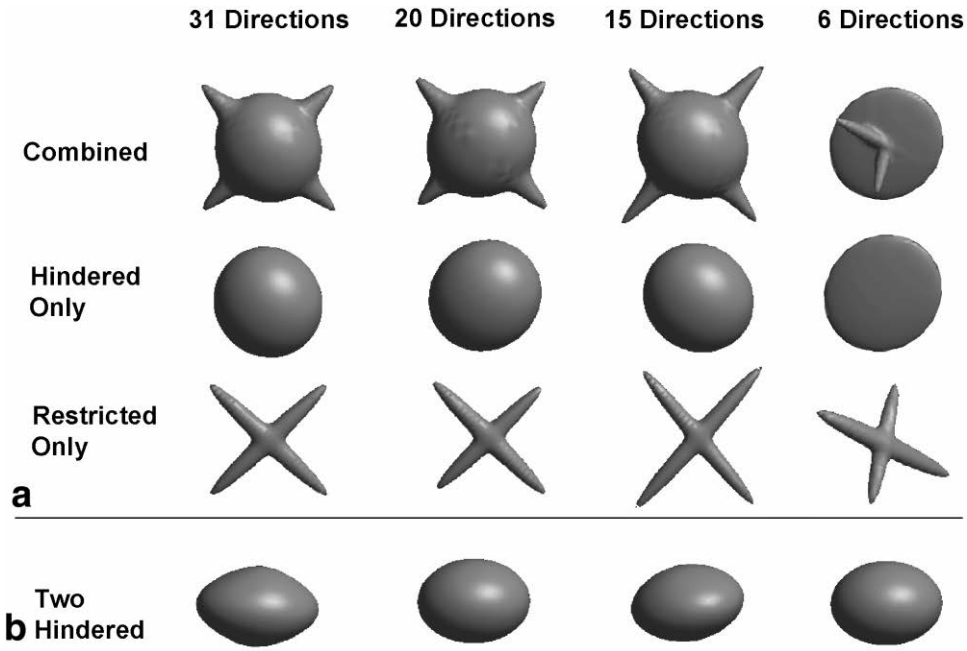

FIG. 5. The displacement iso-probability plots for two fibers crossing at an angle of 90° as a function of number of gradient directions (6, 15, 20, and 31 directions). The simulated signal decay was produced using Eq. [15] with two hindered and two restricted compartments. The hindered compartment parameters were $f_{h1} = f_{h2} = 0.35$, $\Phi_{h1} = 90°$, $\varphi_{h1} = 90°$, $\Phi_{h2} = 135°$, $\varphi_{h2} = 90°$, $\lambda_{//} = \lambda_1 = 0.8 \times 10^{-5}$ cm^2/sec, $\lambda_\perp = \lambda_2 = \lambda_3 = 0.3 \times 10^{-5}$ cm^2/sec. The restricted compartment parameters were $f_{r1} = f_{r2} = 0.15$, $\Phi_{r1} = 90°$, $\varphi_{r1} = 90°$, $\Phi_{r2} = 135°$, $\varphi_{r2} = 90°$, $D_{//} = 1 \times 10^{-5}$ cm^2/sec. The noise floor in the simulations was 0.03. (**a**) Fitting of the simulated data to Eq. [15] with one hindered and two restricted compartments. The contributions from the hindered and restricted compartments are shown separately as is their combined contribution, which is obtained from the 3D FFT of the entire signal decay. (**b**) Displacement iso-probability profile obtained by fitting signal decay to Eq. [15] with two hindered component only using only low *b* value data.

ment of the fibers although the error in the fit was small for all gradient schemes (see Table 1). By contrast, the combination of two restricted and one hindered compartments gave satisfactory results only for gradient schemes of 31, 20, and 15 directions. However, when using the 6-direction gradient scheme, the combined model predicted incorrect results for both compartments. The mean residuals and error of the fitting procedure was more than 10 times higher in the 6-direction scheme than in the 31-direction scheme (see Table 1).

As the model combining one hindered and two restricted compartments gave the best results in the case of two fibers crossing at 90°, we challenged it using two fiber populations crossing at a smaller angle (30°). The data were generated similarly to the previous case by simulating two fibers; each having one restricted and one hin-

Table 1
Fitting of a Two Fiber System Crossing at 90° as Function of Number of Simulated Gradient Directions

One hindered + two restricted model					Two hindered (dual tensor)				
No. directions	Simulation values	Fitted values			No. directions	Simulation values	Fitted values		
		31	20	6			31	20	6
f_h	0.7	0.7	0.68	0.53	f_{h1}	0.5	0.49	0.49	0.64
$\lambda_{//}$ [1]	0.8	0.55	0.63	1.06	f_{h2}	0.5	0.51	0.51	0.28
$\lambda_\perp$ [1]	0.3	0.41	0.42	0.43	$\lambda_{//h1}$ [1]	0.8	0.88	0.79	0.85
f_{r1}	0.15	0.15	0.14	0.28	$\lambda_{\perp h1}$ [1]	0.3	0.50	0.55	0.33
f_{r2}	0.15	0.15	0.19	0.13	$\lambda_{//h2}$ [1]	0.8	0.50	0.35	0.27
Φ_{r1}	135	136	135	152	$\lambda_{\perp h2}$ [1]	0.3	0.18	0.21	0.06
φ_{r1}	90	89	95	66	Φ_{h1}	135	72	2	164
Φ_{r2}	45	44	45	116	φ_{h1}	90	109	5	92
φ_{r2}	90	92	88	26	Φ_{h2}	45	4	−3	8
$D_{//}$ [1]	1	0.89	0.84	0.81	φ_{h2}	90	77	97	187
Noise floor	0.03	0.03	0.024	0.005					
Fit error[2]	—	7.58	12.5	32.8	Fit error	—	18.1	21.5	25.3

[1] $\lambda_{//}$ is the biggest eigenvalue (λ_1) and $\lambda_\perp$ is the average of λ_2 and λ_3 given in $\times 10^{-5}$ cm^2/sec.
[2] Fit error is calculated by the sum of the *z* scores of each of the fitted parameters.

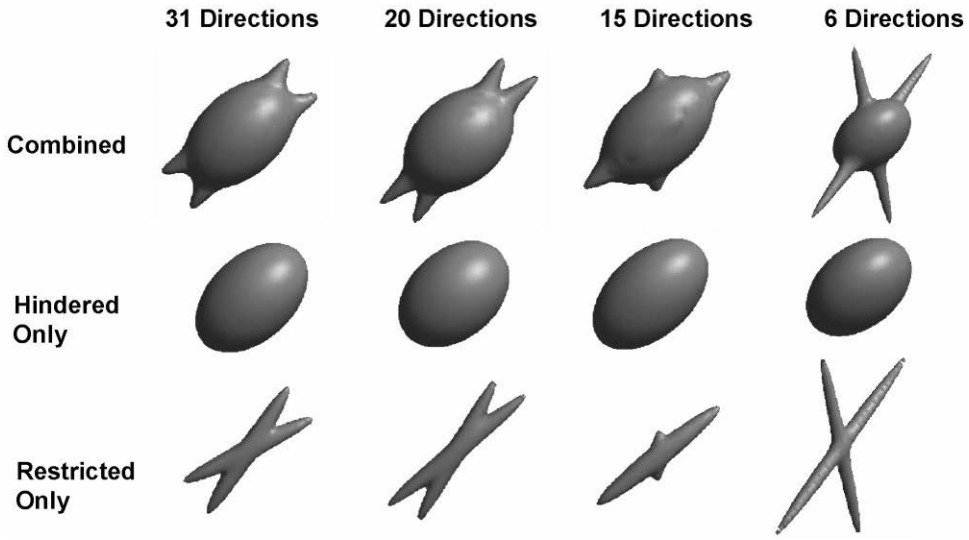

FIG. 6. The displacement iso-probability plots for two fibers crossing at an angle of 30° as a function of number of gradient directions (6, 15, 20, and 31 directions). The simulated signal decay was produced using Eq. [15] with two hindered and two restricted components. The hindered component parameters were $f_{h1} = f_{h2} = 0.35$, $\Phi_{h1} = 30°$, $\varphi_{h1} = 90°$, $\Phi_{h2} = 60°$, $\varphi_{h2} = 90°$, $\lambda_{//} = \lambda_1 = 0.8\ \mu m^2/msec$, $\lambda_\perp = \lambda_2 = \lambda_3 = 0.3 \times 10^{-5}\ cm^2/sec$. The restricted component parameters were $f_{r1} = f_{r2} = 0.15$, $\Phi_{r1} = 30°$, $\varphi_{r1} = 90°$, $\Phi_{r2} = 60°$, $\varphi_{r2} = 90°$, $D_{//} = 1 \times 10^{-5}\ cm^2/sec$. The noise floor in the simulations was 0.03. Displacement iso-probability plots are shown for the hindered compartment only, the restricted compartment alone, and a combination of the two.

dered compartment. Only when using the 31-gradient direction scheme was it possible to separate the two fiber populations accurately (see Fig. 6 and Table 2). The error in the fit increased significantly as the number of sampled directions decreased (see Table 2). This error is also manifested in the shape of 3D FFT iso-probability plots given with gradient schemes of 6 and 15 directions, which do not resemble the one obtained using 31 directions.

Further exploring the limits of the model, we estimated the effect of noise on the fitting procedure. For this purpose we generated signals for two crossing fibers aligned at 45° with respect to each other. The data were generated for various values of the noise floor (0.03, 0.09, 0.12, and 0.18). As the noise floor increased, the accuracy of the fit was reduced dramatically (see Fig. 7). When the noise floor was higher than 0.09, i.e., the SNR was below 11, the fitting procedure failed to produce even approximately accurate results (see Fig. 7).

Table 2
Fitting of a Two Fiber System Crossing at 30° as Function of Number of Simulated Gradient Directions

One hindered + two restricted model				
# Directions	Simulation values	Fitted values		
		31	20	6
f_h	0.7	0.69	0.70	0.69
$\lambda_{//}$ [1]	0.8	0.81	0.67	0.57
$\lambda_\perp$ [1]	0.3	0.31	0.31	0.28
f_{r1}	0.15	0.14	0.13	0.13
f_{r2}	0.15	0.17	0.17	0.18
Φ_{r1}	30	26	39	45
φ_{r1}	90	89	91	77
Φ_{r2}	60	58	62	53
φ_{r2}	90	29	87	63
$D_{//}$ [1]	1	0.85	1.28	3.00
Noise floor	0.03	0.023	0.031	0.023
Σ residuals	—	5.33	6.53	26.0

[1] $\lambda_{//}$ is the biggest eigenvalue (λ_1) and $\lambda_\perp$ is the average of λ_2 and λ_3 given in $\times 10^{-5}\ cm^2/sec$.

Experimental Data

The phantom presented in Fig. 2b was used to provide experimental data of single and crossing fiber bundles (segments of pig spinal cord). The spinal cord segments crossed at 45° to each other. The collected data (up to b value of 44000 sec/mm^2) was fitted using the four combinations of the model given under Methods. Typical fits of data are depicted in Fig. 8, showing the quality of the experimental data and the fits. In Fig. 8 the data were fitted using combination 2 (see Methods).

The diffusion tensor model (one hindered component only) gave accurate results in areas where there was a single fiber bundle (see Fig. 9 and Table 3). In areas of crossing fibers, the diffusion tensor model provided the mean orientations of the two fiber bundles (Fig. 9). Surprisingly, the fractional anisotropy calculated from the diffusion tensor in this regime was not significantly lower in the area of the crossing fiber (see Table 3). The dual tensor model, which a priori has the chance of separating two-fiber orientations, failed to detect the two fiber populations. The dual tensor model (two hindered components) gave reasonable results (data not shown) in only 3 of 33 pixels in the region of crossing fibers. In all other pixels, this model predicted two identical fibers aligned in the mean of two fiber bundles similar to the conventional diffusion tensor model result. It should be noted that with the standard diffusion tensor model and the dual tensor model, the data were analyzed only at the low b value range ($b < 3000$ sec/mm^2).

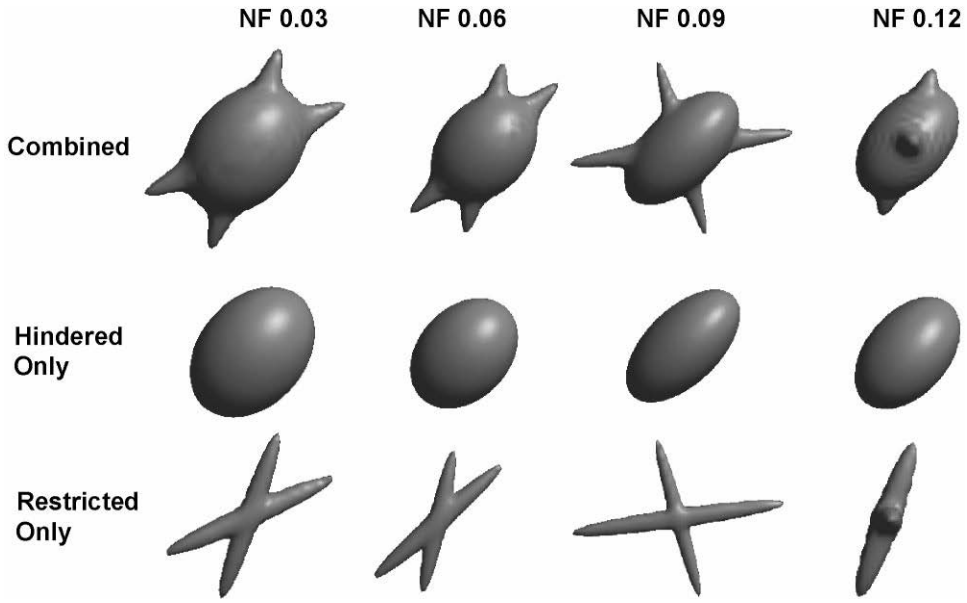

FIG. 7. The displacement iso-probability plots for two fibers crossing at an angle of 45° between them as function of the noise floor. The signal decay was produced using Eq. [15] with two hindered and two restricted compartments. The hindered compartment parameters were $f_{h1} = f_{h2} = 0.35$, $\Phi_{h1} = 25°$, $\varphi_{h1} = 90°$, $\Phi_{h2} = 70°$, $\varphi_{h2} = 90°$, $\lambda_{//} = \lambda_1 = 0.8 \times 10^{-5}$ cm^2/sec, $\lambda_\perp = \lambda_2 = \lambda_3 = 0.3 \times 10^{-5}$ cm^2/sec. The restricted component parameters were $f_{r1} = f_{r2} = 0.15$, $\Phi_{r1} = 25°$, $\varphi_{r1} = 90°$, $\Phi_{r2} = 70°$, $\varphi_{r2} = 90°$, $D_{//} = 1 \times 10^{-5}$ cm^2/sec. The noise floor was incremented from 0.03 to 0.12. The simulated signal decay was fitted using Eq. [15] with one hindered component and two restricted components. Displacement iso-probability plots are shown for the hindered compartment only, the restricted compartment alone, and a combination of the two.

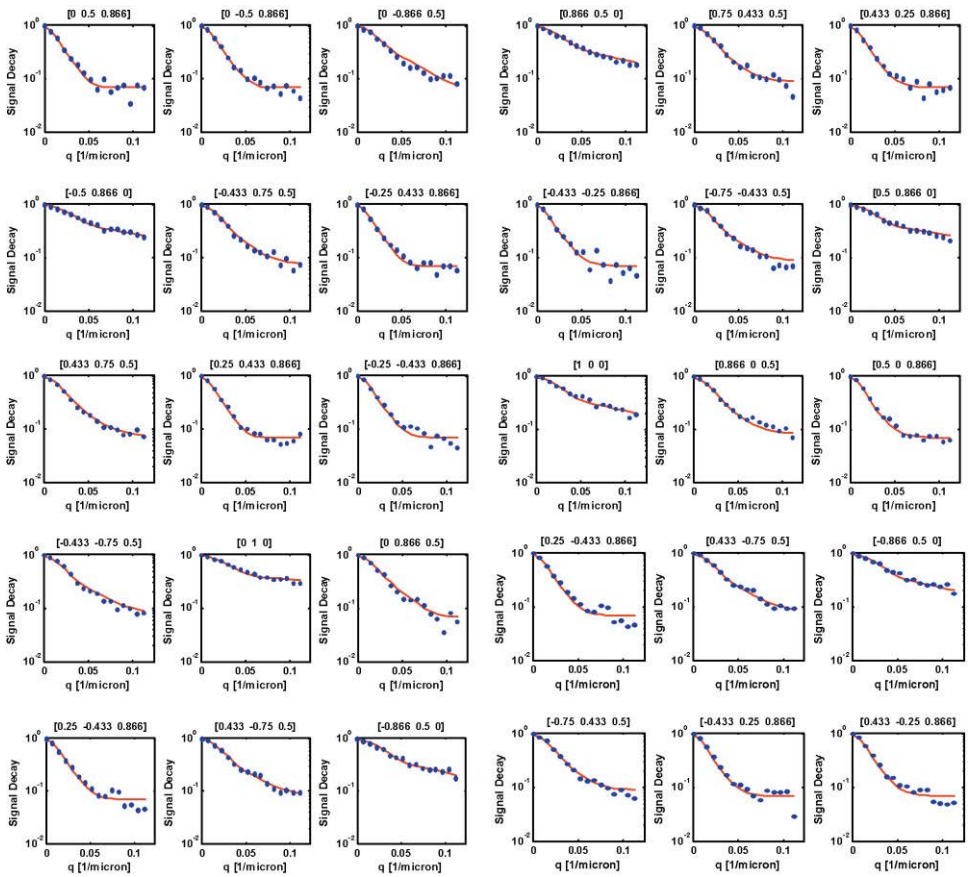

FIG. 8. Typical experimental data taken from one pixel in an area of homogeneous white matter of a pig spinal cord. Data are shown in red and the fit by the model (using one hindered and one restricted components) is shown in blue.

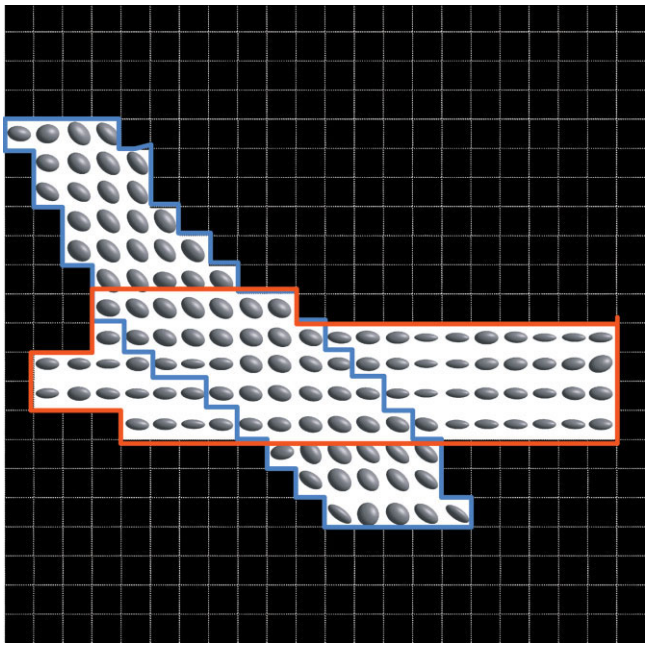

FIG. 9. The displacement iso-probability plots calculated for each pixel in the spinal cord phantom shown in Fig. 2b. The iso-probability plots are calculated from fitting the experimental signal decay (at low *b* values) to Eq. [15] with only one hindered component (identical to conventional diffusion tensor analysis). The red line represents borders of the region containing fibers aligned with the *z*-axis; the blue line represents borders of the region containing fibers aligned 45° below the *z*-axis. The ellipsoids are oriented along the dominant fiber directions in the nonoverlapping regions, but not in the region where fibers cross. For numerical results from the fits, see Table 3.

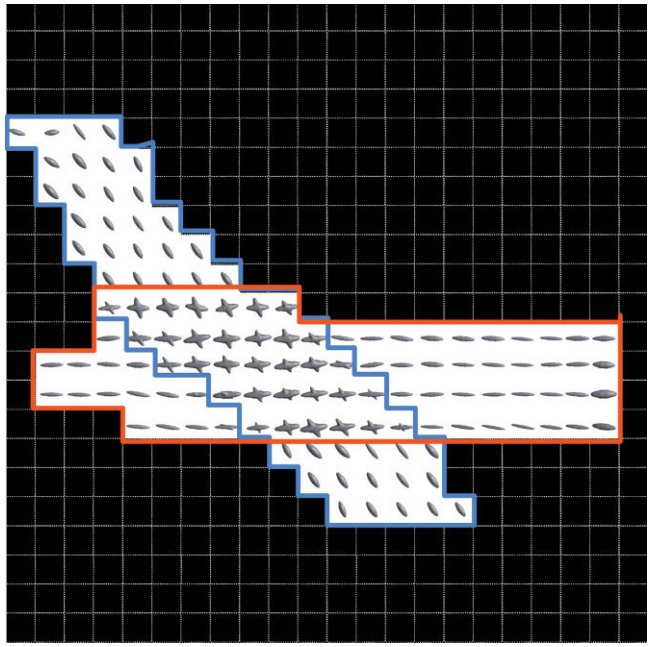

FIG. 10. The displacement iso-probability plots calculated for each pixel in the spinal cord phantom shown in Fig. 2b. In areas where only one fiber population was present, the iso-probability plots were calculated after fitting the entire experimental signal decay to Eq. [15] with one hindered component and one restricted component. In areas of crossing fibers the iso-probability plots were calculated after fitting the experimental signal decay to Eq. [15] with one hindered component and two restricted components. The red line represents the borders of the fiber aligned with the *z*-axis and the blue line represents the borders of the fiber aligned 45° below the *z*-axis. For numerical results from the fits, see Table 3.

In pixels containing a single fiber bundle we also applied CHARMED with single hindered and restricted compartments, where we used the entire signal decay up to the maximal *b* value. Here, the correspondence between the orientations of the hindered and restricted fiber orientations that were computed and that were known from the actual fibers (See Fig. 10 and Table 3) was almost one to one. The other extracted parameters (diffusion eigenvalues) were typical of dead neuronal tissue. Due to the success of this model in separating crossing fibers in the

Table 3
Fitting Results of Spinal Cord Phantom Data

Model	45° fiber		90° fiber		Crossing pixels		
					1h2r[1]		1h[1]
	1h1r[1]	1h[1]	1h1r[1]	1h[1]	45° fiber	90° fiber	
f_h	0.75 ± 0.05	—	0.63 ± 0.06	—	0.68 ± 0.04		—
λ_1 [2]	0.54 ± 0.15	0.34 ± 0.07	0.88 ± 0.24	0.44 ± 0.10	1.48 ± 0.10		0.34 ± 0.05
λ_2 [2]	0.13 ± 0.05	0.14 ± 0.03	0.19 ± 0.05	0.12 ± 0.03	0.51 ± 0.14		0.13 ± 0.02
λ_3 [2]	0.07 ± 0.04	0.10 ± 0.03	0.09 ± 0.03	0.09 ± 0.02	0.11 ± 0.05		0.10 ± 0.02
ϕ_h	80 ± 5	79 ± 5	86 ± 7	88 ± 6	10 ± 2		82 ± 6
φ_h	49 ± 7	50 ± 7	87 ± 5	88 ± 5	89 ± 4		74 ± 6
f_r	0.21 ± 0.03	—	0.36 ± 0.05	—	0.08 ± 0.03	0.23 ± 0.05	—
ϕ_r	77 ± 6	—	88 ± 5	—	73 ± 22	83 ± 6	—
φ_r	47 ± 6	—	92 ± 7	—	44 ± 11	104 ± 4	—
Noise	0.10 ± 0.02	—	0.11 ± 0.03	—	0.09 ± 0.04		—
FA	0.78 ± 0.12	0.60 ± 0.10	0.80 ± 0.07	0.72 ± 0.09	0.78 ± 0.05		0.58 ± 0.08
N	42	42	45	45	27		27

[1]1h model is a single hindered component (i.e., diffusion tensor analysis), 1h 1r is a combination of one hindered and one restricted component, and 1h 2r is a model having combination of one hindered and two restricted components.
[2]λ_1 represents $\lambda_{//}$ whereas λ_2 and λ_3 represents $\lambda_\perp$ given in $\times 10^{-5}$ cm^2/sec.

simulations (see above), in regions of crossing fibers we also tested the combination of two restricted and one hindered compartment. Indeed, this model was able to extract the orientations there (see Fig. 10). The measured fiber orientations were only slightly different from the true values (numerical data given in Table 3).

DISCUSSION

The model presented here attempts to combine and synthesize signal intensity information collected at low and high b (or q) values. In these two experimental regimes, different water pools contribute to the signal decay. The model characterizes diffusion in neuronal tissue as arising from hindered and restricted diffusion processes. While hindered diffusion predominates in the extra-axonal spaces, restricted diffusion in white matter is expected to arise from intra-axonal diffusion (37). It is important to note that by intra-axonal diffusion we mean diffusion within the axoplasm and not between individual layers of the myelin sheath. Our simulations and experimental data support the hypothesis that restricted diffusion within axons might better delineate fiber orientation and even help identify regions where fibers cross.

Our approach differs in important respects from other methods that attempt to provide information about crossing fibers, such as diffusion spectrum imaging (DSI) and high angular resolution diffusion imaging (HARD). While DSI has the advantage of not imposing any explicit model of the diffusion process, it is more data intensive and less informative about the underlying tissue microstructure and organization. The current implementation of HARD only treats data acquired over a sphere in the low b value range, neglecting useful information at moderate and high b values.

Theoretical Aspects

To our knowledge, this is the first modeling approach that provides a 3D description of restricted diffusion suitable for biologic or clinical applications. Motion in the principal and laboratory frames is related functionally so that complex biologic structures can be studied within an imaging volume.

CHARMED is based on the assumption that the motions of molecules parallel and perpendicular to the fiber are statistically independent. This is valid only for certain classes of restricted diffusion, for instance, for diffusion within a tube or between parallel plates. It is not a generally true, however, and in particular is not expected to hold if the boundaries are irregular (or fractal) or when, for instance, there is significant partial refection at the boundaries. The form of Eq. [3] is valid only in the local principal frame, which is the only frame in which these motions parallel and perpendicular to the reflecting wall are uncorrelated. This is why it is important to formulate our diffusion problem in this preferred local frame of reference where the description of diffusive motion is simple and tractable.

The two diffusing components (hindered and restricted) are weighted by a population fraction factor. It is important to distinguish the T_2-weighted volume fractions of the hindered and restricted compartments in this model from the extracellular and intracellular volume fractions reported, for example, using iontophoretic measurements (38). The hindered compartment could include contributions from glia and astrocytes. The f_h and f_r reported here also may arise from compartments with different T_2's or even a spectrum of T_2's, so they do not necessarily reflect true extra- and intracellular volume fractions.

Experimental Aspects

This modeling framework has important implications for DTI tractography. In the context of this model, one hindered and one restricted compartment whose principal axes are aligned with each other should effectively describe coherently organized nerve pathways (see Figs. 4, 9, and 10). We assume here that in homogenously oriented white matter in which neuronal fibers are aligned approximately in the same direction, both hindered and restricted components share the same principal axes. In this circumstance, DTI-based methods can track fibers reliably since the principal axes of the estimated diffusion tensor are an excellent proxy for the principal axes of the restricted nerve fiber. However, in regions with two or more distinct noncollinear restricted compartments, **D** measured using DTI predictably represents a powder average of diffusion tensors from the various hindered compartments (7). In this case, tractography might provide better results when following the principal directions of the restricted compartments (see crossing fibers area in Figs. 9 and 10) rather than the principal direction (eigenvector) associated with the largest eigenvalue provided by DTI.

In contrast to DTI, powder averaging does not take place in multiple restricted compartments. The contribution of each can be separated since the motion within each fiber is independent of the other. Indeed, this is the case seen in our simulations where the restricted model was able to distinguish between fibers crossing at angles as small as 30°. Moreover, using the spinal cord phantom, we were able to show that CHARMED can distinguish between fibers crossing at 45°, although with lower accuracy than in our simulations (see Table 3). One of the many reasons that can contribute to this diminished accuracy is the minimum number of gradient directions needed to define a fiber orientation. It might be that under the limitations of the noise floor level and the pathologic condition of the spinal cord, more gradient directions are needed to measure fiber orientation accurately. This point will be explored in depth in the future.

The model itself provides not only the direction of the fibers, but also other diffusion-related parameters such as the principal diffusivities for the various compartments and the T_2-weighted population fractions. The majority of the signal in DTI arises from the hindered part (about 70%, see Table 3), at least in the freshly excised pig spinal cord. In some subtle white matter disorders, a DTI assessment might be complemented by information from restricted compartments. It has been shown that characterization of the restricted diffusion can extend the diagnostic ability of diffusion imaging (21,22). Quantitative characterization of restricted diffusion in neuronal tissue might help one follow the pathologic mechanisms that underline certain white matter disorders.

Using CHARMED for diffusion data obtained from human brain is more challenging. Given the variety of tissue types and architectures in the brain, it is sensible to use a parsimonious model selection procedure when choosing among the various multicompartment models described above. In this way, one can use the model that most efficiently fits the diffusion decay data on a voxel-by-voxel basis (39). Other limitations that should be explored before clinical application to this model to the human brain could be studied are: (1) the low SNR at high b value that might cause insufficient signal for accurate assessment of fiber orientations and (2) the need for high angular resolution (>20 gradient directions) might cause extremely long acquisition times. However, 4–5 years ago it was believed that diffusion imaging on human brain with b values above 2000 sec/mm^2 was not possible or applicable. Yet, with advances in diffusion gradient hardware it is now possible to reach b values of 20000 and provide informative images that are not corrupted by excessive noise. At the moment it is true that a b value of 44000 sec/mm^2 (as used in the present paper) is not reasonable on a human scanner, but our experience so far with human data showed that it might be sufficient to use b values of up to 15000 sec/mm^2 to obtain similar results; however, this must be further explored.

SUMMARY AND CONCLUSION

We propose a model of water diffusion in white matter having hindered diffusion in the extra-axonal compartment and restricted diffusion in the intra-axonal compartment. The form of the composite model is greatly simplified by observing that displacements in the direction perpendicular and parallel to the restrictive boundary can be uncoupled. From experimental $E(\mathbf{q})$ data, microstructual parameters (e.g., $D_{//}$, $\lambda_{//}$, $\lambda_{\perp}$) can be estimated. From the best fit to $E(\mathbf{q})$ data, a 3D displacement probability distribution, $p(\mathbf{r})$, can be calculated using Callaghan's q-space methodology.

The determination of the orientation(s) of the restricted compartment(s) might provide improved angular resolution and fiber direction(s), which should aid tractography studies. This was shown to be true at least for single fibers. This combined theoretical and experimental framework should provide new parameters that will allow us to follow subtle changes occurring in white matter in disease, development, aging, and degeneration with greater specificity and selectivity. Yet, the implementation of this experimental framework on human scanners is challenging mainly due to signal-to-noise and scanning time limitations.

APPENDIX A

This derivation shows how statistical independence of displacements parallel and perpendicular to a restrictive barrier leads to a simple product relationship between the MR signals due to motion in these orthogonal directions.

Substituting $\mathbf{R} = \mathbf{R}_{//} + \mathbf{R}_{\perp}$ and Eq. [3] into Eq. [2] we obtain

$$E_r(\mathbf{q}, \Delta) = \iiint \bar{P}_{\perp}(\mathbf{R}_{\perp}, \Delta)\bar{P}_{//}(\mathbf{R}_{//}, \Delta)e^{i2\pi\mathbf{q}\cdot(\mathbf{R}_{\perp}+\mathbf{R}_{//})}\, d\mathbf{R}_{\perp}\, d\mathbf{R}_{//}. \quad [A1]$$

The exponents above can now be separated as

$$E_r(\mathbf{q}, \Delta) = \iiint \bar{P}_{\perp}(\mathbf{R}_{\perp}, \Delta)e^{i2\pi\mathbf{q}\cdot\mathbf{R}_{\perp}}\, d\mathbf{R}_{\perp}\bar{P}_{//}(\mathbf{R}_{//}, \Delta)e^{i2\pi\mathbf{q}\cdot\mathbf{R}_{//}}\, d\mathbf{R}_{//} \quad [A2]$$

and the integrals can be factored as well:

$$E_r(\mathbf{q}, \Delta) = \iint \bar{P}_{\perp}(\mathbf{R}_{\perp}, \Delta)e^{i2\pi\mathbf{q}\cdot\mathbf{R}_{\perp}}\, d\mathbf{R}_{\perp} \int \bar{P}_{//}(\mathbf{R}_{//}, \Delta)e^{i2\pi\mathbf{q}\cdot\mathbf{R}_{//}}\, d\mathbf{R}_{//}. \quad [A3]$$

The first integral above describes the signal caused by 2D motion perpendicular to the tube wall while the second integral describes the signal caused by 1D motion parallel to the tube axis.

Now substituting the relationship, $\mathbf{q} = \mathbf{q}_{//} + \mathbf{q}_{\perp}$ in [A3] above, we obtain

$$E_r(\mathbf{q}, \Delta) = \iint \bar{P}_{\perp}(\mathbf{R}_{\perp}, \Delta)e^{i2\pi(\mathbf{q}_{//}+\mathbf{q}_{\perp})\cdot\mathbf{R}_{\perp}}\, d\mathbf{R}_{\perp} \times \int \bar{P}_{//}(\mathbf{R}_{//}, \Delta)e^{i2\pi(\mathbf{q}_{//}+\mathbf{q}_{\perp})\cdot\mathbf{R}_{//}}\, d\mathbf{R}_{//}. \quad [A4]$$

Using the additional requirements that $\mathbf{q}_{//}\cdot\mathbf{R}_{\perp} = \mathbf{q}_{\perp}\cdot\mathbf{R}_{//} = 0$, we obtain Eq. [5] above.

APPENDIX B

Computation of Components of q Parallel and Perpendicular to the Nerve Fiber Axis

The parallel and perpendicular components of q for a single restricted compartment are given by

$$|\mathbf{q}_{\perp}| = |\mathbf{q}|\sqrt{1 - (\sin(\theta_q)\sin(\theta_N)\cos(\varphi_q - \varphi_N) + \cos(\theta_q)\cos(\theta_N))^2} \quad [B1]$$

or

$$|\mathbf{q}_{\perp}|^2 = |\mathbf{q}|^2(1 - (\sin(\theta_q)\sin(\theta_N)\cos(\varphi_q - \varphi_N) + \cos(\theta_q)\cos(\theta_N))^2) \quad [B2]$$

and

$$|\mathbf{q}_{//}| = |\mathbf{q}| \times \sin(\theta_q)\sin(\theta_N)\cos(\varphi_q - \varphi_N) + \cos(\theta_q)\cos(\theta_N) \quad [B3]$$

or

$$|\mathbf{q}_{//}|^2 = |\mathbf{q}|^2 \times (\sin(\theta_q)\sin(\theta_N)\cos(\varphi_q - \varphi_N) + \cos(\theta_q)\cos(\theta_N))^2. \quad [B4]$$

Above, $\theta_q$and φ_q are the spherical coordinates as given by Goldstein (40), indicating the pitch from the *z*-axis and the angular rotation of the *q* vector about the *z*-axis in the *x*–*y* plane, as shown in Fig. 1. θ_N and φ_N, are the spherical coordinates of the axon or nerve fascicles, whose orientation is usually not known.

In the case in which there are two or more restricted compartments, we can identify a particular θ_N^i and φ_N^i for each compartment.

APPENDIX C

The quadratic form, $\mathbf{q}^{\mathrm{T}}\,\mathbf{D}\,\mathbf{q}$, appearing in the cylindrically symmetric hindered model in Eq. [11], can be simplified by substituting $\mathbf{q} = \mathbf{q}_{//} + \mathbf{q}_{\perp}$, keeping in mind that $\mathbf{q}_{\perp} \cdot \mathbf{q}_{//} = 0$:

$$\mathbf{q}^T\mathbf{D}\mathbf{q} = (\mathbf{q}_{\perp} + \mathbf{q}_{//})^T\mathbf{D}(\mathbf{q}_{\perp} + \mathbf{q}_{//}) = \mathbf{q}_{\perp}^T\mathbf{D}\mathbf{q}_{\perp} + \mathbf{q}_{//}^T\mathbf{D}\mathbf{q}_{//} + \mathbf{q}_{\perp}^T\mathbf{D}\mathbf{q}_{//} + \mathbf{q}_{//}^T\mathbf{D}\mathbf{q}_{\perp} = \mathbf{q}_{\perp}^T\mathbf{D}\mathbf{q}_{\perp} + \mathbf{q}_{//}^T\mathbf{D}\mathbf{q}_{//}. \quad [C1]$$

We see that terms such as $\mathbf{q}_{\perp}^T\mathbf{D}\mathbf{q}_{\perp}$ and $\mathbf{q}_{//}^T\mathbf{D}\mathbf{q}_{//}$ above represent projections of the diffusion tensor along $\mathbf{q}_{\perp}$ and $\mathbf{q}_{//}$, respectively. If we further assume, as we did provisionally above, that the eigenvectors (i.e., the principal axes) of the diffusion tensor in the hindered compartment are aligned with the parallel and perpendicular axes of the restricted compartment, then

$$\mathbf{q}^T\mathbf{D}\mathbf{q} = \mathbf{q}_{\perp}^T\mathbf{D}\mathbf{q}_{\perp} + \mathbf{q}_{//}^T\mathbf{D}\mathbf{q}_{//} = \mathbf{q}_{\perp} \cdot \mathbf{q}_{\perp}\lambda_{\perp} + \mathbf{q}_{//} \cdot \mathbf{q}_{//}\lambda_{//} = |\mathbf{q}_{\perp}|^2\lambda_{\perp} + |\mathbf{q}_{//}|^2\lambda_{//}. \quad [C2]$$

A similar decomposition is shown in (17) for cylindrically symmetric anisotropic diffusion.

APPENDIX D

Justification for invoking the statistical independence of the net displacement distribution can be seen by considering Eq. [1]. We can extend the formalism of Cheng and Cory (41) by writing the net signal from the restricted compartment as resulting from the composition of individual random jumps as

$$E_r(\mathbf{q}, \Delta) = \int\int\int \cdots \int\int\int \rho(\mathbf{0}) \prod_{i=1}^{N} P(\mathbf{R}_i, \tau_i\,\mathbf{R}_{i-1}, \tau_{i-1}) e^{i2\pi\mathbf{q}\cdot(\mathbf{R}_i - \mathbf{R}_{i-1})}\, d\mathbf{R}_{i-1}^3, \quad [D1]$$

where $P(\mathbf{R}_i, \tau_i|\mathbf{R}_{i-1}, \tau_{i-1})$ is the conditional probability that a particle originally at $\mathbf{R}_{i\text{-}1}$ at time $\tau_{i\text{-}1}$ will be at position $\mathbf{R}_i$ at time τ_I and ρ° is the spin density.

We can simplify the form of the exponent above,

$$E_r(\mathbf{q}, \Delta) = \int\int\int \cdots \int\int\int e^{i2\pi\mathbf{q}\cdot\sum_{i=1}^{N}{}^{1}(\mathbf{R}_i - \mathbf{R}_{i-1})}\rho(\mathbf{0}) \times \prod_{i=1}^{N} P(\mathbf{R}_i, \tau_i\,\mathbf{R}_{i-1}, \tau_{i-1})\, d\mathbf{R}_{i-1}^3, \quad [D2]$$

and recognize it as the net displacement, **R,** over a time Δ, that results from *N* individual jumps. For microscopic diffusive motions viewed in the principal frame, jumps along the directions parallel and perpendicular to the restrictive boundary are uncorrelated, a common assumption made in performing Monte Carlo simulations:

$$P(\mathbf{R}_i, \tau_i|\mathbf{R}_{i-1}, \tau_{i-1}) = P(x_i, y_i, \tau_i|x_{i-1}, y_{i-1}, \tau_{i-1})P(z_i, \tau_i|z_{i-1}, \tau_{i-1}). \quad [D3]$$

In the case of motions within a restricted tube (where *x* and *y* lie within the plane of the tube's cross-section and *z* lies along the tube's axis), Eqs. [D2] and [D3] become

$$E_r(\mathbf{q},\Delta) = \int\int\int \cdots \left(\int\int e^{i2\pi(q^x \sum_{i=1}^{N}(x_i - x_{i-1}) + q_y \sum_{i=1}^{N}(y_i - y_{i-1}))} \times \prod_{i=1}^{N} P(x_i, y_i, \tau_i|x_{i-1}, y_{i-1}, \tau_{i-1})P(x_0, y_0 = 0, 0)\, dx_i\, dy_i \right) \times \left(\int e^{i2\pi q_z \sum_{i=1}^{N}(z_i - z_{i-1})} \prod_{i=1}^{N} P(z_i, \tau_i|z_{i-1}, \tau_{i-1})P(z_0 = 0)\, dz_i \right). \quad [D4]$$

The sums in the exponents are simply components of the net displacement in the *x*, *y*, and *z* directions.

If we define the average propagator as in Kärger et al. (25),

$$\bar{P}(\mathbf{R}, \Delta) = P(\mathbf{R}, \Delta)P(\mathbf{R} = 0, \Delta = 0), \quad [D5]$$

we can rewrite Eq. [D4] as

$$E_r(\mathbf{q}, \Delta) = \left(\int\int \bar{P}(\mathbf{R}_{\perp}, \Delta|0, 0)e^{i2\pi\mathbf{q}\cdot\mathbf{R}_{\perp}}\, d\mathbf{R}_{\perp} \right) \times \left(\int \bar{P}(\mathbf{R}_{\parallel}, \Delta|\mathbf{0}, 0)e^{i2\pi\mathbf{q}\cdot\mathbf{R}_{\parallel}}\, d\mathbf{R}_{\parallel} \right). \quad [D6]$$

So, if we make the reasonable assumption that the individual molecular jump probabilities parallel and perpendicular to the axis of the restriction are independent, it follows that the net displacement probabilities parallel and perpendicular to the axis of the restriction are independent as well.

REFERENCES

1. Le Bihan D, Basser PJ. Molecular diffusion and nuclear magnetic resonance. In: Le Bihan D, editor. Diffusion and Perfusion Magnetic Resonance Imaging. New York: Raven Press; 1995. p 5–17.

2. Moseley ME, Cohen Y, Kucharczyk J, Mintorovitch J, Asgari HS, Wendland MF, Tsuruda J, Norman D. Diffusion-weighted MR imaging of anisotropic water diffusion in cat central nervous system. Radiology 1990;176(2):439–445.
3. Pajevic S, Pierpaoli C. Color schemes to represent the orientation of anisotropic tissues from diffusion tensor data: application to white matter fiber tract mapping in the human brain. Magn Reson Med 1999; 42(3):526–540.
4. Basser PJ, Mattiello J, Le Bihan D. MR diffusion tensor spectroscopy and imaging. Biophys J 1994;66(1):259–267.
5. Basser PJ, Pierpaoli C. Microstructural and physiological features of tissues elucidated by quantitative-diffusion-tensor MRI. J Magn Reson B 1996;111(3):209–219.
6. Pierpaoli C, Jezzard P, Basser PJ, Barnett A, Di Chiro G. Diffusion tensor MR imaging of the human brain. Radiology 1996;201(3):637–648.
7. Basser PJ, Jones DK. Diffusion-tensor MRI: theory, experimental design and data analysis—a technical review. NMR Biomed 15(7–8):456–467, 2002.
8. Stanisz GJ, Szafer A, Wright GA, Henkelman RM. An analytical model of restricted diffusion in bovine optic nerve. Magn Reson Med 1997; 37(1):103–111.
9. Niendorf T, Dijkhuizen RM, Norris DG, van Lookeren Campagne M, Nicolay K. Biexponential diffusion attenuation in various states of brain tissue: implications for diffusion-weighted imaging. Magn Reson Med 1996;36(6):847–857.
10. Assaf Y, Cohen Y. Non-mono-exponential attenuation of water and N-acetyl aspartate signals due to diffusion in brain tissue. J Magn Reson 1998;131(1):69–85.
11. Mulkern RV, Gudbjartsson H, Westin CF, Zengingonul HP, Gartner W, Guttmann CR, Robertson RL, Kyriakos W, Schwartz R, Holtzman D, Jolesz FA, Maier SE. Multi-component apparent diffusion coefficients in human brain. NMR Biomed 1999;12(1):51–62.
12. Tuch DS, Reese TG, Wiegell MR, Makris N, Belliveau JW, Wedeen VJ. High angular resolution diffusion imaging reveals intravoxel white matter fiber heterogeneity. Magn Reson Med 2002;48(4):577–582.
13. Bossart EL, InglisBA, Buckley DL, Wirth III ED, Mareci TH. Multiple component diffusion tensor imaging in excised fixed CNS tissue. In: Proceedings of the 7th Annual Meeting of ISMRM, Philadelphia, 1999. p 328.
14. Clark CA, Le Bihan D. Water diffusion compartmentation and anisotropy at high b values in the human brain. Magn Reson Med 2000;44(6): 852–859.
15. Boss BC, Stejskal EO. Anisotropic diffusion in hydrated vermiculite. J Chem Phys 1965;43:1068–1069.
16. Assaf Y, Cohen Y. Assignment of the water slow-diffusing component in the central nervous system using q-space diffusion MRS: implications for fiber tract imaging. Magn Reson Med 2000;43(2):191–199.
17. Callaghan PT. Principles of nuclear magnetic resonance microscopy. Oxford: Oxford University Press; 1991.
18. Cory DG, Garroway AN. Measurement of translational displacement probabilities by NMR: an indicator of compartmentation. Magn Reson Med 1990;14(3):435–444.
19. King MD, Houseman J, Gadian DG, Connelly A. Localized q-space imaging of the mouse brain. Magn Reson Med 1997;38(6):930–937.
20. Assaf Y, Kafri M, Shinar H, Chapman J, Korczyn AD, Navon G, Cohen Y. Changes in axonal morphology in experimental autoimmune neuritis as studied by high b-value q-space ^{1}H and ^{2}H DQF diffusion magnetic resonance spectroscopy. Magn Reson Med 2002;48(1):71–81.
21. Assaf Y, Mayzel-Oreg O, Gigi A, Ben-Bashat D, Mordohovitch M, Verchovsky R, Reider G, II, Hendler T, Graif M, Cohen Y, Korczyn AD. High b value q-space-analyzed diffusion MRI in vascular dementia: a preliminary study. J Neurol Sci 2002;203–204:235–239.
22. Assaf Y, Ben-Bashat D, Chapman J, Peled S, Biton IE, Kafri M, Segev Y, Hendler T, Korczyn AD, Graif M, Cohen Y. High b-value q-space analyzed diffusion-weighted MRI: application to multiple sclerosis. Magn Reson Med 2002;47(1):115–126.
23. Quirk JD, Bretthorst GL, Duong TQ, Snyder AZ, Springer CS, Ackerman JJH, Neil JJ. Equilibrium water exchange between the intra- and extracellular spaces of mammalian brain. Magn Reson Med 2003;50(3):493–499.
24. Assaf Y, Mayk A, Cohen Y. Displacement imaging of spinal cord using q-space diffusion-weighted MRI. Magn Reson Med 2000;44(5):713–722.
25. Kärger J, Pfeifer H, Heink W. Principles and applications of self-diffusion measurements by nuclear magnetic resonance. In: Waugh J, editor. Advances in Magnetic Resonance, Vol 12. New York: Academic Press; 1988. p 1–89.
26. Crank J. The mathematics of diffusion. Oxford, UK: Oxford University Press; 1975. 414 p.
27. Stejskal EO. Use of spin echoes in a pulsed magnetic-field gradient to study restricted diffusion and flow. J Chem Phys 1965;43(10):3597–3603.
28. Robertson B. Spin-echo decay of spins diffusing in a bounded region. Phys Rev 1966;151(1):273–277.
29. Neuman CH. Spin echo of spins diffusing in a bounded medium. J Chem Phys 1974;60:4508–4511.
30. Codd SL, Callaghan PT. Spin echo analysis of restricted diffusion under generalized gradient waveforms: planar, cylindrical, and spherical pores with wall relaxivity. J Magn Reson 1999;137(2):358–372.
31. van Gelderen P, DesPres D, van Zijl PC, Moonen CT. Evaluation of restricted diffusion in cylinders. Phosphocreatine in rabbit leg muscle. J Magn Reson B 1994;103(3):255–260.
32. Basser PJ, Mattiello J, Le Bihan D. Estimation of the effective self-diffusion tensor from the NMR spin echo. J Magn Reson B 1994;103(3):247–254.
33. Basser PJ. Relationships between diffusion tensor and q-space MRI. Magn Reson Med 2002;47(2):392–397.
34. Basser PJ. Testing for and exploiting microstructural symmetry to characterize tissues via diffusion tensor MRI. In: Proceedings of the 4th Annual Meeting of ISMRM, New York, 1996. p 1323.
35. Pierpaoli C, Basser PJ. Toward a quantitative assessment of diffusion anisotropy. Magn Reson Med 1996;36(6):893–906.
36. Jones DK. Determining and visualizing uncertainty in estimates of fiber orientation from diffusion tensor MRI. Magn Reson Med 2003;49:7–12.
37. Beaulieu C. the basis of anisotropic water diffusion in nervous system—a technical review. NMR Biomed 15(7–8):435–455, 2002.
38. Nicholson C, Phillips JM, Gardner-Medwin AR. Diffusion from an iontophoretic point source in the brain: role of tortuosity and volume fraction. Brain Res 1979;169(3):580–584.
39. Shrager RI, Jones DK, Pajevic S, Munson P, Basser PJ. When is a Gaussian displacement distribution adequate to describe water diffusion in tissues?; St. Malo, France; 2002.
40. Goldstein H. Classical Mechanics. Reading, MA: Addison-Wesley; 1980. 672 p.
41. Cheng Y, Cory DG. Multiple scattering by NMR. J Am Chem Soc 1999;121(34):7935–7936.